

1 **1. Introduction**

2 Graphene nanoplates (GNPs) are mainly consisted of two-dimensional carbon nano-layers
3 stacked together, which, if being used as the reinforcement, can be considered to have the similar
4 physical properties with those of the single-layer graphene used in metal matrix composites
5 (MMCs) [1-4]. More importantly, the GNPs are much easier to prepare at a larger scale using a
6 liquid-phase chemical reduction method, which makes the GNPs one of the best reinforcement
7 materials for the MMCs [2, 5-7]. So far many studies showed that adding the GNPs into the
8 various MMCs have achieved good mechanical properties (such as those of Al [8, 9], Cu [6, 10],
9 Mg [11] and Ti [5, 12] based ones). The strength has been remarkably increased using the GNPs
10 and the ductility is maintained in a high level without significant deterioration. However, it is still
11 a critical challenge to improve homogeneous dispersion and interfacial bonding of GNPs in
12 MMCs.

13 With the demands for light weight and energy saving in aerospace industry, titanium matrix
14 composites (TMCs) have been considered as the preferred structural materials [13-18].
15 Introducing GNPs into the titanium alloys is a good way to improve their strength, wearability and
16 corrosion performance. However, it is difficult to homogeneously disperse the GNPs and prevent
17 severe *in-situ* interfacial reactions for the GNPs reinforced TMCs during their fabrication process
18 [5, 16]. It is well known that these GNPs (with large surface areas and high surface energy) are
19 prone to agglomerate due to strong van der Waals forces among the GNPs [19-21]. Moreover, the
20 significant *in-situ* reactions and formation of TiC during the sintering process could completely
21 destroy the nano-structures of GNPs, thus leading to a limited strengthening effect [22].

22 Recently, many new types of fabrication methods for improving uniform distribution of

1 fillers and preventing severe interfacial reactions are applied to fabricate TMCs, such as
2 molecular-level mixing [10], chemical vapor deposition [21], and slurry blending [23]. Generally,
3 these reported approaches can be divided into two categories depending on their technologies. One
4 of the most effective ways to inhibit the severe interfacial reactions is to modify the surface of
5 GNPs using chemical vapor deposition or electro-deposition methods [10, 21, 24], and coat the
6 GNPs with various metal nanoparticles (Ni [14], Cu [25, 26] and Ag [26, 27] et.al). For example,
7 Mu et al [14] fabricated nickel coated GNPs (Ni@GNPs) using an electroless plating method, then
8 dispersed these Ni@GNPs into Ti matrix in order to prevent severe interfacial reactions. Results
9 showed that the composite with Ni@GNPs achieved a high strength without significant
10 deterioration of its ductility, which is mainly attributed to the effective interfacial load transfer
11 capability. Li et al [21] showed that the decorated GNPs with Ni nanoparticles not only prevented
12 agglomeration of the GNPs, but also improved bonding strength of the graphene/copper
13 composites. Luo et al [27] applied Ag nanoparticles instead of Ni nanoparticles to coat onto the
14 surfaces of reduced graphene oxides (RGOs), and results showed a significant enhancement of
15 both the interfacial strength and mechanical properties of the Cu composites. However, there is a
16 clear drawback for this method. The multi-step preparation processing is complex,
17 time-consuming, and expensive for large-scale commercial production. It also involves harmful
18 additives/solvents which could weaken the interface adhesion of the composites.

19 The other reported and effective approaches are based on ball milling processes [16, 20, 28],
20 which result in structural destruction of graphene and related materials and severe interfacial
21 reactions. However, due to their simple and perfect operating processes, the ball-milling methods
22 are still the dominant technique to fabricate the MMCs in industry applications [1, 10, 29, 30].

1 Previous studies [24, 31, 32] revealed that the increased wettability between graphene and metal
2 matrix can improve the uniform distribution of graphene and interfacial bonding strength, thus
3 achieving a good interfacial load transfer capability. However, it needs to find solutions in order to
4 disperse the graphene uniformly in the Ti matrix and control the interfacial reactions and
5 orientation alignment of reinforcements in the microstructure during these ball-milling processes.

6 In this study, we adopted a low energy and wet ball milling process to uniformly disperse and
7 align the GNPs in the Ti matrix, and also used a short time and high-temperature spark plasma
8 sintering (SPS) technique to limit the severe interfacial reactions. It is expected that this modified
9 preparation method can maintain the graphene in the Ti matrix after SPS process, and form
10 discontinuous TiC nanoparticles/TiC@GNPs strips-like networks in the TMCs. The mechanisms
11 of the reinforcement effects using GNPs based on the new processes are investigated in detail in
12 this paper.

13 **2. Experimental**

14 **2.1. Raw materials**

15 The GNPs used in this study were provided by Nanjing XFNANO Materials Tech Ltd
16 (Nanjing City, Jiangsu Province, China). As shown in Fig. S1, the GNPs are about 1-5 nm in
17 thickness, and the flake diameters are from 1 to 3 μm . The CT20 alloy with a nominal composition
18 of Ti-3Al-3Zr-1Mo is a near- α titanium alloy (designed by Northwest Institute for Nonferrous
19 Metal Research, China), which was developed for services as low temperature structural materials
20 for aerospace industry. In this study, the high-purity CT20 powders with spherical shapes were
21 fabricated using a rotary electrode method, and the particle diameters are in the range of 50~120
22 μm . The chemical compositions of CT20 powders are listed in Table S1. The chemicals used with

1 analytical grades were all purchased from Aladdin Industrial Corporation.

2 **2.2. Fabrication of bulk GNPs/CT20 composites**

3 The fabrication process for the bulk GNPs/CT20 composites is illustrated in Fig. S2. It is
4 mainly consisted of two steps: (I) uniform distribution of GNPs on the surfaces of spherical Ti
5 powders, and (II) SPS consolidation process. Detail fabrication process are explained as follows.

6 Firstly, the GNPs was dispersed into an alcoholic solution with ultrasonic stirring for 1 h, and then
7 CT20 powders were slowly added into the GNPs suspended solution under a constantly
8 mechanical stirring to form CT20 slurries. Secondly, the mixed GNPs/CT20 slurries were sealed
9 into an agate jar packed with agate milling balls. The ball milling time was fixed at 2 hours with a
10 revolution speed of 260 r/min. Finally, the mixed slurry was completely dried using a vacuum
11 oven, and then the mixtures were manually ground inside the agate mortar to obtain the loose
12 GNPs/CT20 powders. By adjusting the amounts of GNPs, different composite powders with 0.05
13 wt.%, 0.1 wt.%, 0.3 wt.% of GNPs were obtained.

14 The SPS technique offers fast heating/cooling rates (> 500 °C/min) and high sintering
15 efficiency to fabricate the bulk metal matrix composites. The as-prepared GNPs/CT20 composite
16 powders were sintered into discs with 60 mm in diameter using the SPS at 1000 °C for 6 min
17 under a vacuum condition. The compressive pressure applied to the samples was 60 MPa (± 0.02
18 MPa). The sintering temperature was monitored using an infrared thermometry system positioned
19 in the hole of the Mo alloy mold which was located 2 mm away from the sample.

20 **2.3. Material characterization**

21 For microstructural analysis, the surfaces of the samples were mechanically polished using a
22 standard metallographic procedure and then etched in a solution of water, nitric acid, and

1 hydrofluoric acid (with the volume ratio of 5:3:1). Microstructural characterizations were
2 performed using a field-emission scanning electron microscope (FE-SEM, JEOL, JSM-6700F,
3 Japan) equipped with an energy-dispersive spectrometer (EDS), and also a transmission electron
4 microscope (TEM, JEOL, JEM-2100). X-ray diffraction (XRD, D8, ADVANCE) analysis for the
5 phase composition was operated at 30 kV and 30 mA with CuK_α radiation. The chemical bonding
6 structures of graphene and TiC phase in the powders and bulk composites were investigated using
7 both the Raman spectroscopy (Renishaw in Via Reflex, excitation laser 514 nm) and X-ray
8 photoelectron spectroscopy (XPS, ESCALAB, 250Xi). The microstructural analysis (such as
9 volume fraction and grain size) was carried out using the image analysis software of Image J, and
10 each sample was repeated three times to ensure a good accuracy.

11 **2.4. Tensile test**

12 Room temperature tensile tests were carried out using a universal testing machine (Instron
13 598X) at a constant crosshead speed of 1 mm/min. Dog bone-shaped specimens with a gauge
14 length of 12 mm and gauge width of 4 mm were prepared using an electro-discharge machining
15 technique. In order to confirm the validity of tensile results, tensile tests of each sample were
16 repeated twice. After the tensile test, the fracture surfaces were observed using the SEM equipped
17 with EDS.

18 **3. Results and discussion**

19 **3.1. Characterization of the powders**

20 Fig. 1 shows SEM morphologies of CT20 powders used in this work. The spherical CT20
21 powders exhibit a bimodal size distribution with an average diameter of 72.43 μm . This bimodal
22 distribution is beneficial for the full densification of CT20 powders during the SPS, as the fine

1 particles can be filled into the spaces in the triangle intersection of coarse powders in the SPS
2 process. EDS analysis shows that the CT20 powders contain 1.92 wt.% Al, 2.32 wt.% Zr and 1.03
3 wt.% Mo, which are consistent with the results obtained using a chemical method (Inductively
4 coupled plasma mass spectrometry (ICP-MS), Table S1). The EDS mapping images (Fig. 1(e) ~
5 Fig. 1(h)) display that all of the alloying elements are homogeneously distributed inside the CT20
6 powders, meaning that the Al, Zr and Mo atoms are completely solid-solubilized in the Ti lattice
7 without the formation of Ti segregates or Ti-Al eutectoid phases.

8 Figs. 2(a) ~ Fig. 2(c) show SEM images of the distribution of GNPs on CT20 powder surface.
9 The GNPs/CT20 composite powders retain a good spherical shape, and the GNPs with many
10 wrinkles are unfolded and homogeneously distributed on powders surfaces, forming a
11 quasi-continuously core-shell microstructure. Fig. 2(d) and Fig. 2(e) show the Raman
12 spectroscopy and EDS results of the composite powders. The characteristic peaks for graphene (D
13 peak at 1350 cm^{-1} , G peak at 1580 cm^{-1} and 2D peak at 2670 cm^{-1}) are all obtained in the spectrum
14 of GNPs/CT20 powders. The relative intensity ratio between the D and G peaks (I_D/I_G) can be
15 used to show the ratio of defects in the graphene, and the I_{2D}/I_G was obtained to analyze the
16 dispersion of graphene and the number of graphene layer [7, 14, 19]. It is found that a high I_D/I_G
17 ratio (1.65) and a low I_{2D}/I_G ratio (0.31) were obtained for the GNPs@CT20 powders after the low
18 energy/wet ball milling. This indicates that there are many types of defects (such as GNPs
19 deformation, high density crack propagation zone, folding zone and the expansion of the original
20 defect) and multi-layer features of GNPs formed on the CT20 powders surface. Some of these
21 defects can be observed in Fig. 2(b).

22 3.2. Microstructure of bulk GNPs/CT20 composites

1 Mechanical properties of TMCs are not only determined by the volume fraction and types of
2 reinforcements, but also affected by the microstructure of matrix and the directional alignment of
3 reinforcements. XRD patterns of GNPs/CT20 composites (Fig. S3) show that the composites are
4 consisted of hexagonal close-packed α phase and small amount of body-centered cubic β phase.
5 No GNPs or other new phases (such as TiC) are detected owing to a small amount of GNPs or few
6 carbides formed during SPS. Fig. 3 shows SEM images of GNPs/CT20 composite reinforced with
7 different GNPs, and the distribution results of prior β grains are also inserted. It can be seen that
8 the microstructure of CT20 matrix consists of lath-shaped α phases, α phase at grain boundaries
9 (α_G) and intergranular β phases. Many α plates around 0.6-4 μm in width are parallel to each other
10 along a specific habit plane. Their average volume fraction and length-width ratio are 85.60 % and
11 15.20, which forms α colonies and distributes in the prior β grains.

12 Fig. 4 shows TEM and HRTEM images of the CT20 matrix. The lath-shaped α phases have a
13 Burgers orientation relationship with the adjacent β matrix, which can be expressed as $[110]_\alpha //$
14 $[-101]_\beta$. This microstructure is typical for the sintered TMCs alloys within the $\alpha+\beta$ temperature
15 region, and belongs to the classical Widmanstatten microstructure reported in literature [33]. In
16 addition, the β grains of all the samples have equiaxed shapes. The GNPs and *in-situ* formed TiC
17 phases are distributed at the grain boundaries, and they become slightly aggregated with the
18 increase of GNP contents (Fig. 3(g)). The average grain size of 0.3% GNPs/CT20 composite is
19 about 61.28 μm , which is much smaller than that of pure CT20 sample (107.00 μm). This result
20 confirms that the GNPs as a reinforcement are effective in refining matrix grains due to their
21 uniform quasi-distributions and blocking effects.

22 According to Ti-C phase diagram [5, 19], the solubility limit of carbon in α -Ti phase is less

1 than 0.8 wt.%, and in β -Ti phase is also less 0.48 wt.%. GNPs as a carbon element will be
2 unavoidably dissolved into Ti matrix. Meanwhile, some carbides (TiC_x) can form from
3 carbonization reactions between Ti matrix and GNPs during the high temperature SPS process.
4 Fig. 5(a) and Fig. 5(b) show SEM images of 0.3 wt.% GNPs/CT20 composite in both the
5 secondary electron mode and backscattered electron mode, respectively. Results show that the
6 reinforcement in GNPs/CT20 composites is comprised of not only *in situ* formed TiC, but also the
7 surrounding structures of TiC@GNPs. TiC particles and TiC@GNPs structure can be observed at
8 grain boundaries (Fig. 5(b)), with discontinuous distribution patterns. These TiC particles have
9 equiaxial shapes, and their average sizes are about 600 nm. Some TiC particles become aggregated
10 together to form the strips of TiC (Fig. 5(g)). Other TiC particles are surrounded on the surfaces of
11 GNPs (Fig. 5(c)). Therefore, the GNPs distributed in the center of *in situ* TiC strips are formed as
12 the “core” structures. They have been restrained due to a shielding effect from the dense TiC layer,
13 thus forming an irregular “sandwich” structure (e.g., TiC@GNPs). In this study, no obviously
14 accumulated regions of TiC particles or TiC@GNPs have been observed in 0.05/0.1 wt%
15 GNPs/CT20 composites (Fig. 3(c) - Fig. 3(f)), probably due to the low content of GNPs. Fig. 5(c)
16 ~ Fig. 5(j) show the high-magnification SEM images with the corresponding EDS analysis for TiC
17 particles and TiC@GNPs structures, which can confirm the existence of TiC phase. Therefore,
18 these reinforcements (e.g., TiC particles, TiC concentration strips and TiC@GNPs strips) can
19 effectively restrict the growth of β grains and also improve the strength properties due to their
20 strong pinning effect.

21 The presence of TiC and GNPs can be further verified from the XPS and Raman
22 spectroscopy analysis. The XPS survey spectra of 0.3 wt.% GNPs/CT20 composite is shown in

1 Fig. 6(a). The peaks located at 284.5 and 455.5 eV are those of Ti2p and C1s. Fig. 6(b) shows the
2 high resolution XPS Ti 2p spectrum where two main components at 453.8 and 459.95 eV are
3 corresponding to Ti 2p_{3/2} and Ti 2p_{1/2}. In addition, the satellite peaks at 454.6 and 460.2 eV are
4 corresponding to the bonding energy of Ti-C bonds, which confirms the existence of TiC phases
5 [34]. Fig. 6(c) presents the high resolution XPS C 1s spectrum. Three major components are
6 indexed as C=C (sp² 284.5 eV), C-C (sp³ 284.4 eV) and C-O (285.3 eV) of the GNPs. Meanwhile,
7 the chemical bonding between GNPs and Ti is also obtained at the 281.97 eV, well consistent with
8 the reported sp²-hybridized carbon orbitals of TiC [34].

9 As shown in the Raman spectra of the 0.3 wt.% GNPs/CT20 composites (Fig. 6(d)), the
10 obtained I_D/I_G and I_{2D}/I_G ratios are 0.36 and 0.46. The I_D/I_G ratio of the sintered sample
11 significantly decreases but I_{2D}/I_G only slightly increases in compared with those of the mixed
12 GNPs/CT20 powders. This clearly shows the lower defect concentration in the GNPs and the
13 few-layered graphene-like GNPs in the composites. Therefore, short time and high-temperature
14 SPS technique can be effective to control the interfacial reactions, which is critical for fabricating
15 the high performance TMCs.

16 **3.3. Interfacial structure and formation mechanism in GNPs/CT20 composites**

17 SEM observation shows that *in-situ* formed TiC phases and TiC@GNPs strips are mainly
18 located around grain boundaries. In order to further analyze the microstructures and evolution of
19 interfacial structures, TEM and HRTEM analysis were carried out. Fig. 7 shows typical TEM and
20 HRTEM images of the interfaces between TiC and Ti matrix. It can be observed that the *in-situ*
21 TiC phases are well bonded with CT20 matrix, which can strengthen the bonding interfaces. No
22 impurities, voids, and gaps are observed at the interfaces between TiC and Ti matrix. As shown in

1 the bright-field TEM images (Fig. 7(a) and Fig. 7(b)), many TiC particles are nucleated and grown
2 along prior grain boundaries during the carburization reactions. This causes the formation of a thin
3 TiC interface layer because the few-layer GNPs are surrounded the CT20 powders surface. Fig.
4 7(c) shows the SAED pattern of TiC phase (position A in Fig. 7(b)). The diffraction pattern of TiC
5 shows the [-101] zone of face-centered cubic NaCl-type structure. The disappearance of GNPs in
6 this zone indicates that the GNPs have been completely reacted with Ti to form titanium carbides
7 (TiC) during the SPS process.

8 Fig. 7(d) displays the HRTEM image of the TiC/Ti matrix interface which clearly shows the
9 nanostructures and crystallographic orientation. A high magnification view as an inset in Fig. 7(d)
10 shows no other carbides, indicating the formation of a strong interfacial bonding. The fast Fourier
11 transform (FFT) and inverse fast Fourier transform (IFFT) results of the selected area in Fig. 7(d)
12 are used to analyze the interfacial layer. The FFT image (Fig. 7(e)) confirms the presence of (111)
13 and (-1-1-1) planes of TiC phase. The lattice inter-planar spacing in IFFT image (Fig. 7(f)) is
14 ~ 0.2455 nm, which is best matched with the d-spacing of (111)_{TiC} plane. These results confirm
15 that TiC has the crystal relation with α -Ti matrix of $[111]_{\text{TiC}} // [11-1]_{\alpha\text{-Ti}}$. This proves the strong
16 bonding between TiC and Ti matrix, which can provide effective load-bearing and transfer
17 capacity [14, 22, 23]. Therefore, the *in-situ* formed TiC could not only achieve the compact
18 interfacial bonding, but also provide the reinforcement effect to strengthen the composites.

19 Fig. 8 shows the bright field TEM image and the corresponding HRTEM image for
20 TiC/GNPs interface in 0.3% GNPs/CT20 composite. There is large-area overlapping of GNPs
21 around 50 nm in the thickness which are evenly and closely anchored inside the dense CT20 Ti
22 matrix. Abundant nano-sized TiC particles (15-60 nm in diameters) can be observed on the

1 surfaces of GNPs (Fig. 8(a)), forming the surrounding structures of TiC@GNPs. Fig. 8(b) shows
2 the corresponding SAED pattern of the GNPs sheets and nano-sized TiC particles (Fig. 8(a)).The
3 discontinues ring-like patterns in the center circle can be identified to be the face-centered cubic
4 NaCl-type structure of TiC, with its characteristic (00-2) and (020) diffraction patterns. In addition,
5 the characteristic diffraction patterns of (010) and (100) for GNPs are also detected in the SAED
6 pattern (Fig. 8(b)).

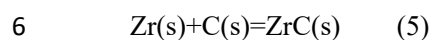
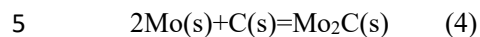
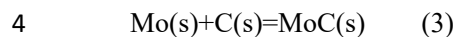
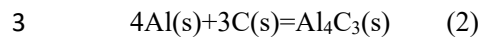
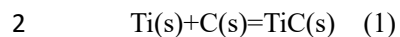
7 In order to well understand the interfacial structure and bonding strength of GNPs/CT20
8 composite during the SPS process, the crystallographic orientation relationship between GNPs and
9 TiC was investigated. The FFT and IFFT diffraction patterns obtained at the surrounding
10 interfacial regions of TiC particles are shown in Fig. 8(d) - Fig. 8(f). A specific orientation
11 relationship at GNPs/TiC interface can be found. Due to the high stiffness of TiC, the planes of
12 $(110)_{\text{TiC}}$ and $(002)_{\text{GNPs}}$ are nearly overlapped with each other along the projection zone axis of
13 $[110]_{\text{TiC}}$ or $[220]_{\text{GNPs}}$, which can be expressed as $[110]_{\text{TiC}} // [220]_{\text{GNPs}}$. According to the IFFT
14 images, the d-spacing of $(002)_{\text{GNPs}}$ is much larger than that of $(110)_{\text{TiC}}$ at the GNPs/TiC interfaces,
15 indicating there is a semi-coherent relationship of interfacial energy. This *in-situ* grown TiC phase
16 has been widely reported in GNPs/Ti composites [13, 29], and its content, particle size and
17 distribution can be controlled by adjusting the SPS parameters. Moreover, the FFT diffraction
18 pattern clearly reveals that there is a coherent GNPs/TiC interface and no other compounds can be
19 detected at the interface. This result, together with the low interfacial energy, prove that *in-situ*
20 formed nano-scale TiC particles not only enhance the interface bonding between GNPs and Ti
21 matrix, but also provide effective load transfer at the interface during the plastic deformation.

22 When various carbon materials as reinforcements (including GNPs, GOs, carbon nanotubes

1 and nanofiber) are induced in TMCs composites during sintering process, the *in-situ* formation of
2 TiC phases is easily obtained due to the solid-solid sintering reactions at high temperatures. We
3 also observe that the *in-situ* formed TiC particles/layers are preferred to nucleate and grow at the
4 structural defect regions of GNPs, and thus bonded with Ti matrix and GNPs without apparent
5 gaps and impurities. This discovery can be confirmed by the comparisons between the Raman
6 spectra of the mixed powders and as-sintered samples (Fig. 2(d) and Fig. 6(d)). The I_D/I_G ratio
7 (which represents the structural defects in GNPs) of as-sintered 0.3 wt.% GNPs/CT20 composites
8 is significantly decreased from 1.65 to 0.36, and the I_{2D}/I_G ratio (which represents the dispersion of
9 GNPs) is only slightly increased from 0.31 to 0.46 in comparison to that of the mixed 0.3 wt.%
10 GNPs/CT20 powders. The defect density of GNPs in GNPs/CT20 powders is quite high due to the
11 deformation and fracture of GNPs as well as generation and propagation of cracks after the ball
12 milling process. The GNPs in GNPs/CT20 composites show much lower defect concentrations,
13 because that the defects in GNPs are preferred to bond with Ti matrix, thus *in-situ* forming TiC
14 during SPS process. As a result, the remained GNPs with much lower defects are covered by the
15 TiC layer to form the core-shell structures at grain boundaries.

16 In this study, the nucleation and growth of *in-situ* formed TiC is mainly based on the GNPs/Ti
17 solid-solid carburization reactions during the high-temperature SPS. As this process is an
18 exothermic process, it can further promote the sintering ability of GNPs/CT20 mixed powders to
19 form the compact GNPs/Ti bonding interfaces. In order to investigate thermodynamics of the
20 carburizing reactions between CT20 matrix and GNPs, the corresponding Gibbs free energy (ΔG ,
21 kJ/mol) and formation enthalpy (ΔH , kJ/mol) of carbide formation at the interfaces were
22 calculated. Due to the existence of alloying elements (such as Al, Mo, Zr) in the CT20 matrix,

1 there could be various carburizing reactions during the sintering process [13, 29]:



7 According to the thermodynamic theory, the Gibbs free energy (ΔG) and reaction formation
8 enthalpy (ΔH) can be obtained based on the following equations [35]:

9 $\Delta G = \Delta G^\theta + RT \ln Q$ (6)

10 $\Delta H = \Delta G + T\Delta S$ (7)

11 where R is the reaction constant, T is the reaction temperature (K), Q (kJ) is the heat losses energy
12 at T , and ΔS is the reaction entropy (kJ/K/mol) [15, 18]. The calculation results for ΔG and ΔH are
13 shown in Fig. S4 as a function of temperature using the thermodynamics data reported in Ref. [36].
14 In this study, the as-prepared GNPs/CT20 composite was sintered at a temperature of 1273 K, and
15 the calculated free energies of the formed carbides are all negative values. The ΔG and ΔH values
16 of the five carbides can be ranked in the following descending order: $\Delta G_{\text{MoC}} < \Delta G_{\text{Mo}_2\text{C}} < \Delta G_{\text{TiC}} <$
17 $\Delta G_{\text{ZrC}} < \Delta G_{\text{Al}_4\text{C}_3}$, and $\Delta H_{\text{MoC}} < \Delta H_{\text{Mo}_2\text{C}} < \Delta H_{\text{TiC}} < \Delta H_{\text{ZrC}} < \Delta H_{\text{Al}_4\text{C}_3}$. Moreover, the ΔG and ΔH
18 values of TiC, Al₄C₃ and ZrC are less than -200 kJ/mol. Here the negative results of ΔG shows
19 that the chemical reaction (e.g., carbide formation) is thermodynamically feasible. The bonding of
20 Al element with C is the strongest among the five carbides. Meanwhile, the obtained negative
21 enthalpy values for the reactions show that the formation of carbides is an exothermic reaction,
22 favoring for the formation of compact bonding interfaces. However, there is only TiC formation

1 observed in the GNPs/CT20 composite. This is probably because the contents of the other alloying
2 elements (including Al, Zr and Mo) in Ti matrix are too low, thus their carbides are difficult to be
3 detected.

4 Based on the above results, *in-situ* formed TiC nanoparticles could enhance densification of
5 microstructures and refine the grain size in the TMCs, both of which are dependent on the bonding
6 interfaces and the barrier formation induced in the discontinuous architectures. Fig. 9 shows our
7 proposed formation mechanism of *in-situ* TiC nanolayers/nanoparticles and TiC@GNPs strips in
8 GNPs/CT20 composite. In the initial stage of SPS process (Fig. 9(a)), the defect region of GNPs
9 (such as deformed GNPs, high density crack propagation zone, folding zone and enlarged original
10 defects) can provide the most active sites for the carbonation reactions. Carbon atoms in these
11 places firstly diffuse and segregate to the adjacent Ti matrix, and then rapidly react with the active
12 Ti atom in these regions to form TiC nanolayers/nanoparticles. The TiC phases are preferred to
13 epitaxially grow along the certain crystal planes in the Ti matrix [13, 15]. With the increase of
14 sintering time (Fig. 9(b)), many carbon atoms in the defect region of GNPs diffuse and accumulate
15 at GNPs/TiC interfaces, thus resulting in fast carburizing reactions, and aggregation of TiC
16 nanoparticles. The defect-free region only has thin TiC nanolayers. The retained GNPs are within
17 the *in situ* formed TiC layer, which forming a shielding effect for the GNPs. This results in the
18 formation of the irregular surrounding structures (TiC@GNPs strips). At the last stage (Fig. 9(c)),
19 the existence of TiC nanolayers/nanoparticles and the TiC@GNPs strips result in the rapid grain
20 refinement. These TiC microstructures and TiC@GNPs strips are uniformly dispersed at grain
21 boundaries, forming discontinuous network microstructures.

22 **3.4. Mechanical properties and strengthening mechanism**

1 Fig. 10(a) presents the typical engineering stress-strain curves of GNPs/CT20 composites. It
2 can be observed that the addition of GNPs into CT20 composites enhances its strength and only
3 slightly deteriorates its ductility. For 0.3 wt.% GNPs/CT20 composite, the ultimate tensile strength
4 (UTS) and yield stress (YS) are increased to 820.97 MPa and 759.71 MPa, which is 27 % and 34%
5 higher than those of pure CT20 composite (647.96 MPa for UTS and 567.77 MPa for YS).
6 Whereas its fracture elongation (E, 21.5 %) is about 11.5 % less than that of pure CT20 (24.4 %).
7 Both the highest values of UTS (986.42 MPa) and YS (924.17 MPa) were obtained in 0.05 wt.%
8 GNPs/CT20 composites, increased up to 52 % and 62.5 % compared with those of pure CT20
9 composite, respectively. When a low content of GNPs is induced in the GNPs/CT20 composites,
10 the GNPs may be completely transformed to TiC nanolayers/nanoparticles during
11 high-temperature SPS, which can significantly increase the strength. This result is consistent with
12 that reported in literature [4, 14, 16].

13 The effects of GNPs contents on the UTS, YS and E are summarized in Fig. 10(b). With the
14 increase of GNPs contents, both values of UTS and YS are continuously decreased. In contrast,
15 the fracture elongation of composites is continually increased with the increased GNPs contents.
16 These tensile test results verify that the *in-situ* formed TiC nanolayers/nanoparticles and the
17 TiC@GNPs strips enhance both UTS and YS values, and improve the ductility.

18 Fig. 10(c) shows the variation of work hardening rate with plastic strain with respect to the
19 increase of GNPs. The work hardening rate obviously increases with increasing GNPs contents,
20 due to the formation of TiC nanoparticles and TiC@GNPs strips. With the increase of GNPs
21 contents, the *in-situ* formed TiC nanolayers/nanoparticles and TiC@GNPs strips are located
22 around the grain boundaries (Fig. 3(h)), thus forming a discontinuous network structure. This kind

1 of structure can overcome the weakening of grain boundaries in the composites, and enhance both
2 the load bearing capability and grain bonding strengthening effect in comparing to the sample with
3 homogenously distributed reinforcements. This observation is similar with that reported by Huang
4 et al [37, 38]. When the composites are deformed, these discontinuous network structures will
5 restrict the movement of dislocations, and cause severe entanglements and pile up of dislocations
6 at the grain boundaries. These lead to the increase of the work hardening effect of the composite.

7 Fig. 11 shows SEM images of the fracture surfaces of pure CT20 and GNPs/CT20
8 composites. The fracture surface of pure CT20 composite (Fig. 11(a) and Fig. 11(b)) is covered by
9 a large number of dimples and a few cleavage planes which are surrounded by tearing ridges. This
10 clearly indicates the typical plastic fracture mode. With gradually increasing the GNPs, the
11 discontinuous network structure in GNPs/CT20 composite can be observed from the fracture
12 surface (Fig. 11(c)), and these TiC nanolayers/nanoparticles and TiC@GNPs strips are dispersed
13 homogeneously at the grain boundary of CT20 matrix. Compared with that of the pure CT20
14 composite, the entire fractured surface of GNPs/CT20 composite is covered by dimples and
15 micro-voids generated at the TiC/GNPs interfaces. Moreover, the micro-voids are deformed along
16 the tensile direction, revealing that the TiC@GNPs structure absorbed a great energy during
17 tensile deformation. The crack is mainly initiated and then propagate from TiC/GNPs interfaces,
18 and this lead to the low fracture elongation rate as the GNPs content is increased. The
19 high-magnification SEM images in Fig. 11(d) - Fig. 11(f) show pull-out phenomena, indicating the
20 strong interface bonding strength and strengthening effect enhanced by the TiC@GNPs strips and
21 TiC nanolayers/nanoparticles.

22 According to the tensile result, a remarkable strengthening effect has been achieved by the

1 discontinuous network structure through the introduction of GNPs. As shown in Fig. 3, the
2 microstructures of the Ti matrix has been changed after adding the different GNPs, indicating that
3 the good performance is mainly associated with the shape, size and distributional characteristic of
4 reinforcements in CT20 composites. One of the variations is that the *in-situ* formed TiC
5 nanoparticles and TiC@GNPs strips are dispersed homogeneously on grain boundary to form the
6 discontinuous network structures. Another important factor is the grain refinement of CT20
7 composites due to the pinning effect of carbides. The increased grain boundary can provide high
8 resistance to dislocation movement [39], which is an important reason for the increased
9 strengthening effect. The improved strength contributed by grain refinement ($\Delta\sigma_{GS}$) can be
10 calculated according to Hall-Petch relationship [40, 41]:

$$11 \quad \Delta\sigma_{GS} = k(d_c^{-0.5} - d_0^{-0.5}) \quad (8)$$

12 where d_c and d_m are the average grain sizes of pure CT20 and GNPs/CT20 composites, and k is 0.4
13 MPa m^{1/2} for the titanium [42-44]. In this study, the measured grain size results for the composites
14 are shown in Fig. 3. The calculated values of $\Delta\sigma_{GS}$ are 0.82 MPa, 5.77 MPa and 12.43 MPa, for
15 GNPs/CT20 composites with the GNPs content from 0.05 wt.% to 0.3 wt.%, respectively. We can
16 see that the strengthening effect due to the grain refinement effect is not as significant, thus it
17 should not be the dominant reason for the enhanced strength.

18 Except grain strengthening, there are several other strengthening mechanisms for the strength
19 improvement, including solution strengthening [45], thermal mismatch strengthening [46],
20 Orowan strengthening [47], *in-situ* formed TiC strengthening [14] and load transfer effects [48,
21 49]. In this study, the solution strengthening by interstitial elements of O, N and H can be ignored
22 due to the short-time ball milling and rapid sintering process. In addition, it is reported that the

1 thermal mismatch between carbon nanomaterials and metal at high temperature can be remained
 2 after quenching [2, 40]. The GNPs/CT20 composites in our work were prepared using the SPS
 3 combined with furnace cooling, which means that the thermal mismatch strengthening ($\Delta\sigma_{TM}$) is
 4 limited. The Orowan strengthening ($\Delta\sigma_{OR}$) is an important strengthening mechanism in the metal
 5 matrix composites. The *in-situ* TiC nanoparticles and TiC@GNPs strips could all pin the
 6 dislocations. The formation of residual dislocation loops around reinforcements can form traps,
 7 which prevents the movement of dislocations, leading to an improvement for strength [48, 50]. The
 8 $\Delta\sigma_{OR}$ can be defined as the follows [5, 51]:

$$9 \quad \Delta\sigma_{OR} = \frac{0.13Gb}{d_c[(\frac{1}{2V_{GNPs}})^{1/3}]} \ln(\frac{d_c}{2b}) \quad (9)$$

10 where b is Burger vector, d_c is the average particle size of TiC nanoparticles and TiC@GNPs
 11 structure, G is the shear modulus of titanium. The length of *in-situ* formed TiC nanolayers and
 12 TiC@GNPs are about 2-15 μ m, and they are mainly distributed at grain boundary, which is the
 13 limitations of estimation for Orowan mechanism. Based on these discussions, the contribution of
 14 Orowan strengthening is not a dominant factor in this study.

15 *In-situ* formed TiC strengthening is the main strength mechanism for GNPs/CT20 composites,
 16 because these *in-situ* TiC particles can enhance both the strength and nano-hardness [12, 14]. In
 17 the GNPs/CT20 composites with a low content of GNPs, the GNPs may be completely
 18 transformed into TiC nanolayers/nanoparticles during high-temperature SPS, which significantly
 19 increase the strength of the composite. Due to the high modulus (450 GPa for elastic modulus) and
 20 hardness (3200 kg/mm for Vickers hardness) for TiC, formation of these massive TiC
 21 nanoparticles will inevitably cause the deterioration of fracture toughness and brittle fracture.
 22 However, the TiC@GNPs structure can be formed in the high GNPs content composites due to the

1 rapid sintering process. This special microstructure can effectively absorb much energy and inhibit
2 the crack propagation during loading process, and exhibit the excellent load transfer effects from
3 the matrix to TiC nanolayers to GNPs, leading to the improvement of mechanical performance for
4 GNPs/CT20 composites. Kelly et.al [52] employed the Shear-lag model to explain the strength
5 mechanism of short fiber reinforced composites, and the deformation stress can be effectively
6 transferred to the fibers through an interfacial stress. Therefore, the high load will be effectively
7 supported by TiC@GNPs strips. The results show that the load transfer strengthening is another
8 main strength mechanism for GNPs/CT20 composites.

9 Based on the above discussion, for GNPs/CT20 composites, the strengthening effects are
10 mainly contributed from the combined strengthening of *in-situ* TiC nanolayers/nanoparticles and
11 load transfer effects. According to the mixing law, the fracture strength of composites can be
12 qualitatively predicted using the following equation [8, 50, 53]:

$$13 \quad \sigma_c = [\Delta\sigma_{lt} + \Delta\sigma_{TiC}] \cdot V_f + \sigma_m \cdot V_m - \Delta\sigma_{int} \quad (10)$$

14 where σ_c , σ_m , $\Delta\sigma_{lt}$, $\Delta\sigma_{TiC}$ and $\Delta\sigma_{int}$ are the strength of the composite, the strength of the CT20
15 matrix, the strength increment due to load transfer, the strength increment by TiC nanoparticles
16 and the internal stress. The internal stress in the MMCs is created due to the coefficient of thermal
17 expansion mismatch between the reinforcements and metal matrix during temperature variations,
18 which has a negative contribution to the strength of matrix [54, 55]. V_f and V_m are the volume
19 fractions of the reinforcement and the matrix, respectively. In this study, the interfacial bonding
20 strength for TiC/GNPs and TiC/CT20 matrix is sufficiently strong to resist debonding during
21 loading. Fig. 11(c) clearly reveals the pull-out phenomenon of GNPs. It is confirmed that the
22 well-preserved GNPs with the *in-situ* formed TiC at interfaces could be effective to improve the

1 interfacial bonding.

2 The present work demonstrates that GNPs/CT20 composites with the discontinuous network
3 structure show both high strength and good ductility, which is beneficial for practical industrial
4 application. According to the mechanism analysis, the strengthen efficiency by GNPs is largely
5 decreased due to the TiC@GNPs strips in comparing to the low content of GNPs, and the detail
6 reason and mechanism analysis is unknown until now. Our future work is aimed to investigate size
7 effect of TiC@GNPs strips and control the interfacial bonding thickness to enhance the
8 mechanical behavior. Quantitative evaluation of TiC strengthening and interfacial evolutions of
9 TiC@GNPs structure using TEM observation will also be further studied.

10 **4. Conclusions**

11 In this study, the high performance GNPs/CT20 composites with the discontinuous network
12 structure were prepared using a short time SPS technology combined low energy/wet ball milling
13 process. The uniform distribution of TiC nanoparticles and the irregular TiC@GNPs strips at grain
14 interface is influenced by GNPs contents. The *in-situ* formed TiC phase not only enhance the
15 strong interface bonding between GNPs and Ti matrix, but also strengthen the composites. This
16 special TiC@GNPs structure combined with the interface of TiC/GNPs/ TiC ($[110]_{\text{TiC}} // [220]_{\text{GNPs}}$)
17 significantly enhances the interface load transfer capability. For mechanical performance, the UTS
18 and YS of 0.3wt.%GNPs/CT20 composite are increased to 820.97 MPa and 759.71 MPa, which is
19 27 % and 34 % higher than those of pure CT20 (647.96 MPa for UTS and 567.77 MPa for YS),
20 and its fracture elongation (21.5 %) is about 11.5 % less than that of pure CT20 (24.4 %). The
21 strength enhancement is mainly attributed to the following two mechanisms: *in-situ* TiC
22 interface/particle strengthening and load transfer effects. The GNPs/CT20 composites in this study

1 have shown both high strength and good ductility, due to formation of these bioinspired multilevel
2 architectures and improved interfacial bonding.

3 **Acknowledgments**

4 This work was performed under the support of the Nation Natural Science Foundation of
5 China (Grant No. U1737108 and 51641107), the Natural Science Foundation of Shaanxi Province
6 (2017JQ5084) and Shaanxi Youth star program of Science and Technology (2020-74). Key
7 Research and Development Projects of Shaanxi Province (No. 2019GY-164), Science and
8 Technology Project of Weiyang District of Xi'an City (No. 201857).

9 **References**

- 10 [1] F. Chen, J. Ying, Y. Wang, S. Du, Z. Liu, Q. Huang, Effects of graphene content on the
11 microstructure and properties of copper matrix composites, *Carbon*, 96 (2016) 836-842.
- 12 [2] J. Li, X. Zhang, L. Geng, Effect of heat treatment on interfacial bonding and strengthening
13 efficiency of graphene in GNP/Al composites, *Composites Part A: Applied Science and*
14 *Manufacturing*, 121 (2019) 487-498.
- 15 [3] L.L. Dong, J.W. Lu, Y.Q. Fu, W.T. Huo, Y. Liu, D.D. Li, Y.S. Zhang, Carbonaceous
16 nanomaterial reinforced Ti-6Al-4V matrix composites: Properties, interfacial structures and
17 strengthening mechanisms, *Carbon*, 164 (2020) 272-286.
- 18 [4] X.N. Mu, H.N. Cai, H.M. Zhang, Q.B. Fan, F.C. Wang, X.W. Cheng, Z.H. Zhang, J.B. Li, X.L.
19 Jiao, Y.X. Ge, S. Chang, L. Liu, Y.N. Liu, Size effect of flake Ti powders on the mechanical
20 properties in graphene nanoflakes/Ti fabricated by flake powder metallurgy, *Composites Part A:*
21 *Applied Science and Manufacturing*, 123 (2019) 86-96.
- 22 [5] X.N. Mu, H.M. Zhang, H.N. Cai, Q.B. Fan, Z.H. Zhang, Y. Wu, Z.J. Fu, D.H. Yu,

- 1 Microstructure evolution and superior tensile properties of low content graphene nanoplatelets
2 reinforced pure Ti matrix composites, *Materials Science and Engineering: A*, 687 (2017) 164-174.
- 3 [6] X. Si, M. Li, F. Chen, P. Eklund, J. Xue, F. Huang, S. Du, Q. Huang, Effect of carbide
4 interlayers on the microstructure and properties of graphene-nanoplatelet-reinforced copper matrix
5 composites, *Materials Science and Engineering: A*, 708 (2017) 311-318.
- 6 [7] A. Azarniya, A. Azarniya, S. Sovizi, H.R.M. Hosseini, T. Varol, A. Kawasaki, S. Ramakrishna,
7 Physicomechanical properties of spark plasma sintered carbon nanotube-reinforced metal matrix
8 nanocomposites, *Progress in Materials Science*, 90 (2017) 276-324.
- 9 [8] M. Khan, R. Ud Din, A. Wadood, W.H. Syed, S. Akhtar, R.E. Aune, Effect of graphene
10 nanoplatelets on the physical and mechanical properties of Al6061 in fabricated and T6 thermal
11 conditions, *Journal of Alloys and Compounds*, 790 (2019) 1076-1091.
- 12 [9] P. Shao, W. Yang, Q. Zhang, Q. Meng, X. Tan, Z. Xiu, J. Qiao, Z. Yu, G. Wu, Microstructure
13 and tensile properties of 5083 Al matrix composites reinforced with graphene oxide and graphene
14 nanoplates prepared by pressure infiltration method, *Composites Part A: Applied Science and
15 Manufacturing*, 109 (2018) 151-162.
- 16 [10] J. Hwang, T. Yoon, S.H. Jin, J. Lee, T.-S. Kim, S.H. Hong, S. Jeon, Enhanced mechanical
17 properties of graphene/copper nanocomposites using a molecular-level mixing process, *Advanced
18 Materials*, 25 (2013) 6724-6729.
- 19 [11] L. Meng, X. Hu, X. Wang, C. Zhang, H. Shi, Y. Xiang, N. Liu, K. Wu, Graphene
20 nanoplatelets reinforced Mg matrix composite with enhanced mechanical properties by structure
21 construction, *Materials Science and Engineering: A*, 733 (2018) 414-418.
- 22 [12] H. Cao, Y. Liang, The microstructures and mechanical properties of graphene-reinforced

- 1 titanium matrix composites, *Journal of Alloys and Compounds*, 812 (2020) 152057.
- 2 [13] V.V. Rielli, V. Amigó-Borrás, R.J. Contieri, Microstructural evolution and mechanical
3 properties of in-situ as-cast beta titanium matrix composites, *Journal of Alloys and Compounds*,
4 778 (2019) 186-196.
- 5 [14] X.N. Mu, H.N. Cai, H.M. Zhang, Q.B. Fan, F.C. Wang, Z.H. Zhang, Y.X. Ge, R. Shi, Y. Wu,
6 Z. Wang, D.D. Wang, S. Chang, Uniform dispersion and interface analysis of nickel coated
7 graphene nanoflakes/ pure titanium matrix composites, *Carbon*, 137 (2018) 146-155.
- 8 [15] M.D. Hayat, H. Singh, Z. He, P. Cao, Titanium metal matrix composites: An overview,
9 *Composites Part A: Applied Science and Manufacturing*, 121 (2019) 418-438.
- 10 [16] L.L. Dong, B. Xiao, Y. Liu, Y.L. Li, Y.Q. Fu, Y.Q. Zhao, Y.S. Zhang, Sintering effect on
11 microstructural evolution and mechanical properties of spark plasma sintered Ti matrix
12 composites reinforced by reduced graphene oxides, *Ceramics International*, 44 (2018)
13 17835-17844.
- 14 [17] J. Lu, Y. Zhao, Y. Du, W. Zhang, Y. Zhang, Microstructure and mechanical properties of a
15 novel titanium alloy with homogeneous (TiHf)₅Si₃ article-reinforcements, *Journal of Alloys and*
16 *Compounds*, 778 (2019) 115-123.
- 17 [18] J. Lu, X. Yang, Y. Zhao, L. Dong, Y. Fu, Y. Du, W. Zhang, Y. Zhang, Influence of α s
18 precipitates on electrochemical performance and mechanical degradation of Ti-1300 alloy, *Journal*
19 *of Alloys and Compounds*, 803 (2019) 88-101.
- 20 [19] K. Chu, F. Wang, X. Wang, Y. Li, Z. Geng, D. Huang, H. Zhang, Interface design of
21 graphene/copper composites by matrix alloying with titanium, *Materials & Design*, 144 (2018)
22 290-303.

- 1 [20] X.N. Mu, H.N. Cai, H.M. Zhang, Q.B. Fan, F.C. Wang, Z.H. Zhang, Y. Wu, Y.X. Ge, S.
2 Chang, R. Shi, Y. Zhou, D.D. Wang, Uniform dispersion of multi-layer graphene reinforced pure
3 titanium matrix composites via flake powder metallurgy, *Materials Science and Engineering: A*,
4 725 (2018) 541-548.
- 5 [21] M. Li, H. Che, X. Liu, S. Liang, H. Xie, Highly enhanced mechanical properties in Cu matrix
6 composites reinforced with graphene decorated metallic nanoparticles, *Journal of Materials*
7 *Science*, 49 (2014) 3725-3731.
- 8 [22] L.L. Dong, B. Xiao, L.H. Jin, J.W. Lu, Y. Liu, Y.Q. Fu, Y.Q. Zhao, G.H. Wu, Y.S. Zhang,
9 Mechanisms of simultaneously enhanced strength and ductility of titanium matrix composites
10 reinforced with nanosheets of graphene oxides, *Ceramics International*, 45 (2019) 19370-19379.
- 11 [23] Z. Hu, G. Tong, Q. Nian, R. Xu, M. Saei, F. Chen, C. Chen, M. Zhang, H. Guo, J. Xu, Laser
12 sintered single layer graphene oxide reinforced titanium matrix nanocomposites, *Composites Part*
13 *B: Engineering*, 93 (2016) 352-359.
- 14 [24] Z. Hu, F. Chen, J. Xu, Z. Ma, H. Guo, C. Chen, Q. Nian, X. Wang, M. Zhang, Fabricating
15 graphene-titanium composites by laser sintering PVA bonding graphene titanium coating:
16 Microstructure and mechanical properties, *Composites Part B: Engineering*, 134 (2018) 133-140.
- 17 [25] K. Zhou, W.G. Chen, J.J. Wang, G.J. Yan, Y.Q. Fu, W-Cu composites reinforced by copper
18 coated graphene prepared using infiltration sintering and spark plasma sintering: A comparative
19 study, *International Journal of Refractory Metals and Hard Materials*, 82 (2019) 91-99.
- 20 [26] A. El-Gendi, F.A. Samhan, N. Ismail, L.A.N. El-Dein, Synergistic role of Ag nanoparticles
21 and Cu nanorods dispersed on graphene on membrane desalination and biofouling, *Journal of*
22 *Industrial and Engineering Chemistry*, 65 (2018) 127-136.

- 1 [27] H. Luo, Y. Sui, J. Qi, Q. Meng, F. Wei, Y. He, Mechanical enhancement of copper matrix
2 composites with homogeneously dispersed graphene modified by silver nanoparticles, *Journal of*
3 *Alloys and Compounds*, 729 (2017) 293-302.
- 4 [28] M. Bastwros, G.Y. Kim, C. Zhu, K. Zhang, S. Wang, X. Tang, X. Wang, Effect of ball milling
5 on graphene reinforced Al6061 composite fabricated by semi-solid sintering, *Composites Part B:*
6 *Engineering*, 60 (2014) 111-118.
- 7 [29] J.L. Li, Y.C. Xiong, X.D. Wang, S.J. Yan, C. Yang, W.W. He, J.Z. Chen, S.Q. Wang, X.Y.
8 Zhang, S.L. Dai, Microstructure and tensile properties of bulk nanostructured aluminum/graphene
9 composites prepared via cryomilling, *Materials Science and Engineering: A*, 626 (2015) 400-405.
- 10 [30] Y. Jiang, Z. Tan, R. Xu, G. Fan, D.B. Xiong, Q. Guo, Y. Su, Z. Li, D. Zhang, Tailoring the
11 structure and mechanical properties of graphene nanosheet/aluminum composites by flake powder
12 metallurgy via shift-speed ball milling, *Composites Part A: Applied Science and Manufacturing*,
13 111 (2018) 73-82.
- 14 [31] M. Cao, D.B. Xiong, Z. Tan, G. Ji, B. Amin-Ahmadi, Q. Guo, G. Fan, C. Guo, Z. Li, D.
15 Zhang, Aligning graphene in bulk copper: Nacre-inspired nanolaminated architecture coupled with
16 in-situ processing for enhanced mechanical properties and high electrical conductivity, *Carbon*,
17 117 (2017) 65-74.
- 18 [32] X. Zhang, C. Shi, E. Liu, N. Zhao, C. He, High-strength graphene network reinforced copper
19 matrix composites achieved by architecture design and grain structure regulation, *Materials*
20 *Science and Engineering: A*, 762 (2019) 138063.
- 21 [33] J. Lu, P. Ge, Q. Li, W. Zhang, W. Huo, J. Hu, Y. Zhang, Y. Zhao, Effect of microstructure
22 characteristic on mechanical properties and corrosion behavior of new high strength Ti-1300 beta

1 titanium alloy, *Journal of Alloys & Compounds*, 727 (2017) 1126-1135.

2 [34] J.R. Rumble, D.M. Bickham, C.J. Powell, The NIST x - ray photoelectron spectroscopy
3 database, *Surface & Interface Analysis*, 19 (1992) 241-246.

4 [35] P. Glansdorff, I. Prigogine, *Thermodynamic theory of structure, stability and fluctuations*,
5 *American Journal of Physics*, 41 (1971) 147-148.

6 [36] I. Barin, O. Knacke, O. Kubaschewski, *Thermochemical properties of inorganic substances*,
7 Springer-Verlag, 1977.

8 [37] L.J. Huang, Y.Z. Zhang, L. Geng, B. Wang, W. Ren, Hot compression characteristics of
9 TiBw/Ti6Al4V composites with novel network microstructure using processing maps, *Materials*
10 *Science and Engineering: A*, 580 (2013) 242-249.

11 [38] S. Wang, L. Huang, Q. An, S. Jiang, R. Zhang, L. Geng, S. Qu, H. Peng, Regulating crack
12 propagation in laminated metal matrix composites through architectural control, *Composites Part*
13 *B: Engineering*, 178 (2019) 107503.

14 [39] R. Casati, M. Vedani, *Metal Matrix Composites Reinforced by Nano-Particles—A Review*,
15 *Metals*, 4 (2014) 65-83.

16 [40] F. Saba, F. Zhang, S. Liu, T. Liu, Reinforcement size dependence of mechanical properties
17 and strengthening mechanisms in diamond reinforced titanium metal matrix composites,
18 *Composites Part B: Engineering*, 167 (2019) 7-19.

19 [41] Y. Guo, T.B. Britton, A.J. Wilkinson, Slip band–grain boundary interactions in
20 commercial-purity titanium, *Acta Materialia*, 76 (2014) 1-12.

21 [42] W.F. Smith, J. Hashemi, *Foundations of Materials Science and engineering*, Mc Graw Hill,
22 2011.

- 1 [43] C.J. Zhang, J.P. Qu, J. Wu, S.Z. Zhang, J.C. Han, M.D. Hayat, P. Cao, A titanium composite
2 with dual reinforcements of micrometer sized TiB and submicrometer sized Y₂O₃, Materials
3 Letters, 233 (2018) 242-245.
- 4 [44] C.J. Zhang, C.X. Guo, S.Z. Zhang, H. Feng, C.Y. Chen, H.Z. Zhang, P. Cao, Microstructural
5 manipulation and improved mechanical properties of a near α titanium alloy, Materials Science
6 and Engineering: A, 771 (2020) 138569.
- 7 [45] M.R. Bache, W.J. Evans, Impact of texture on mechanical properties in an advanced titanium
8 alloy, Materials Science and Engineering: A, 319-321 (2001) 409-414.
- 9 [46] H. Wei, Z. Li, D. B. Xiong, Z. Tan, G. Fan, Z. Qin, D. Zhang, Towards strong and stiff carbon
10 nanotube-reinforced high-strength aluminum alloy composites through a microlaminated
11 architecture design, Scripta Materialia, 75 (2014) 30-33.
- 12 [47] Z. Zhang, D.L. Chen, Consideration of orowan strengthening effect in particulate-reinforced
13 metal matrix nanocomposites: A model for predicting their yield strength, Scripta Materialia, 54
14 (2006) 1321-1326.
- 15 [48] J.G. Park, D.H. Keum, Y.H. Lee, Strengthening mechanisms in carbon nanotube-reinforced
16 aluminum composites, Carbon, 95 (2015) 690-698.
- 17 [49] S.J. Yoo, S.H. Han, W.J. Kim, Strength and strain hardening of aluminum matrix composites
18 with randomly dispersed nanometer-length fragmented carbon nanotubes, Scripta Materialia, 68
19 (2013) 711-714.
- 20 [50] S.C. Tjong, Recent progress in the development and properties of novel metal matrix
21 nanocomposites reinforced with carbon nanotubes and graphene nanosheets, Materials Science
22 and Engineering: R: Reports, 74 (2013) 281-350.

- 1 [51] Z. Zhang, D.L. Chen, Consideration of Orowan strengthening effect in particulate-reinforced
2 metal matrix nanocomposites: A model for predicting their yield strength, *Scripta Materialia*, 54
3 1321-1326.
- 4 [52] A. Kelly, Tensile properties of fiber-reinforced metal: Copper/tungsten and
5 copper/molybdenum, *Journal of the Mechanics & Physics of Solids*, 13 (1965) 329-350.
- 6 [53] X. Zhang, C. Shi, E. Liu, F. He, L. Ma, Q. Li, J. Li, N. Zhao, C. He, In-situ space-confined
7 synthesis of well-dispersed three-dimensional graphene/carbon nanotube hybrid reinforced copper
8 nanocomposites with balanced strength and ductility, *Composites Part A: Applied Science and*
9 *Manufacturing*, 103 (2017) 178-187.
- 10 [54] M. Schöbel, W. Altendorfer, H.P. Degischer, S. Vaucher, T. Buslaps, M.D. Michiel, M.
11 Hofmann, Internal stresses and voids in SiC particle reinforced aluminum composites for heat sink
12 applications, *Composites Science and Technology*, 71 (2011) 724-733.
- 13 [55] Y. Wu, E.J. Lavernia, Strengthening behavior of particulate reinforced MMCs, *Scripta*
14 *Metallurgica et Materialia*, 27 (1992) 173-178.